JACS
JOURNAL OF THE AMERICAN CHEMICAL SOCIETY
Article
pubs.acs.org/JACS

Nanoparticle Assemblies in Supramolecular Nanocomposite Thin Films: Concentration Dependence

Joseph Kao[†] and Ting Xu*[,†,‡,§]

[†]Department of Materials Science & Engineering, University of California, Berkeley, California 94720, United States
[‡]Department of Chemistry, University of California, Berkeley, California 94720, United States
[§]Materials Sciences Division, Lawrence Berkeley National Laboratory, Berkeley, California 94720, United States

Supporting Information

ABSTRACT: The phase behavior of supramolecular nanocomposite thin films was systematically investigated as a function of nanoparticle (NP) loading from 1 to >50 wt %. The coassembly of NP and supramolecule can be divided into five regimes, from a supramolecule-guided assembly to a NP governing assembly process, depending on the energetic contributions from the surface energy, NP-supramolecule interaction, and the kinetic pathway of the assembly process. A range of morphologies such as 1D NP chains, 2D sheets, 3D NP assemblies, and NP solids can be readily obtained, providing opportunities to meet structural control in nanocomposites for a wide range of applications.

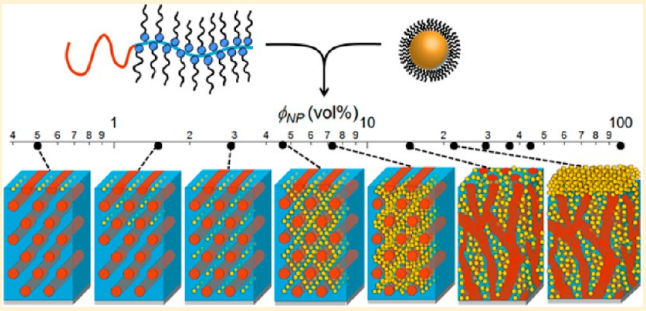

INTRODUCTION

Nanocomposites can combine unique properties of nanoparticles (NPs) and the solution processability of macromolecules. Composites with well-controlled nanostructures are highly desirable to achieve optimal predicted properties.[1,2] However, most studies in polymer/NP blends, where synergistic coassemblies of both components were achieved, focused on fairly low NP loadings, which are often below the critical threshold to achieve percolation required to improve physical properties of the nanocomposites.[1,2] For example, in nanocomposite-based electronics or photovoltaics, efficient electron transport requires the formation of percolation networks, which were estimated to form above 17 vol % NP loading based on 3D continuum models for spherical NPs.[3,4] Nanoparticles of different composition can be synthesized in situ within polymeric framework and the NP loading can be fairly high.[5−12] Nanocomposites can also be obtained via the coassembly of polymers or supramolecule and presynthesized NPs.[13−23] This coassembly approach takes advantage of recent developments in colloidal particle synthesis, allowing the generation of nanocomposites containing NPs of different sizes and chemical compositions. This opens up the possibilities to develop new materials using any elements on the periodic table.

The NP concentration (ϕ_{NP}) is one of the critical parameters governing the collective properties of the composites originating from the overall spatial arrangement of NPs and the interparticle coupling.[12,24−28] The phase behavior of polymer/NP blends as a function of ϕ_{NP}, especially at high ϕ_{NP} regime, needs to be considered from both thermodynamic and kinetic points of view.[13,14,16,17,29] Upon NP incorporation, the polymer chains deform to accommodate them, leading to an entropic penalty.[13,14] At high nanoparticle loadings, it may become too entropically costly to accommodate NPs in the polymeric domains, resulting in particle aggregation/macrophase separation. In the case of block copolymer (BCP)/NP blends, the BCP order will be lost. This can be offset to some extent by reinforcing favorable BCP/NP ligand enthalpic interactions. For example, hydrogen bonding[30−34] and ionic interactions[35] have been employed to strengthen the NP/BCP interactions to increase the volume fraction of NPs without undergoing macrophase separation. As ϕ_{NP} increases, the addition of NPs may induce morphological transitions in the nanocomposites.[36−39] In addition, the nanocomposites may become kinetically trapped due to the jamming of NPs at high ϕ_{NP}.[40,41]

Here, we systematically investigate the phase behavior of supramolecular nanocomposite in thin films with ϕ_{NP} ranging from 0.4 to 45 vol %. The coassembly of NPs and supramolecule can be divided into five regimes, from a supramolecule-guided assembly to a NP governing assembly process. The experimental observations clearly show the interplay among various energetic contributions from the supramolecule, NP, surfaces, etc., and provide useful guidance for future theoretical studies. A range of morphologies can be readily obtained, providing opportunities to attain structural control in nanocomposites for various applications.

Received: March 9, 2015
Published: April 28, 2015

DOI: 10.1021/jacs.5b02494
J. Am. Chem. Soc. 2015, 137, 6356−6365

RESULTS AND DISCUSSION

The supramolecular nanocomposites contain the supramolecule, PS(19 kDa)-*b*-P4VP(5.2 kDa)$(PDP)_{1.7}$ and different amounts of ~4.9 nm Au NPs capped with 1-dodecanethiol. The size analysis of the NPs is shown in Supporting Information (SI) Figure S1 and the details for the preparation of the nanocomposite thin films have been described previously.[42,43] Supramolecular nanocomposite thin films with ϕ_{NP} ranging from 0.4 to 45 vol % (see SI-2) were prepared by spin-casting from the stock solution and solvent annealed under $CHCl_3$ vapor. The solvent annealing condition was controlled such that the films swelled to 145% of their original film thicknesses during the annealing process. The studies were divided into five regimes based on the ϕ_{NP} value, i.e., Regime I: ϕ_{NP} < 3 vol %; Regime II: 3 vol % < ϕ_{NP} < 15 vol %); Regime III: 15 vol % < ϕ_{NP} < 20 vol %; Regime IV: 20 vol % < ϕ_{NP} < 30 vol %; and Regime V: ϕ_{NP} > 30 vol %.

Regime I: 0.4 vol % < ϕ_{NP} < 3 vol %. Figure 1a,b show the AFM and TEM images of a ~200 nm nanocomposite thin film at ϕ_{NP} = 0.4 vol %, respectively. The Au NPs form a single 1D NP chain in the middle of P4VP$(PDP)_{1.7}$ microdomain at the film surface. The top-view TEM image shows fingerprint patterns of NP chains with interarray spacing ~33 nm, which is the lateral periodicity of the supramolecular thin film. Cross-sectional TEM image further confirms that the NPs are localized at the air/film interface, as illustrated in the schematic drawing (Figure 1c,d).

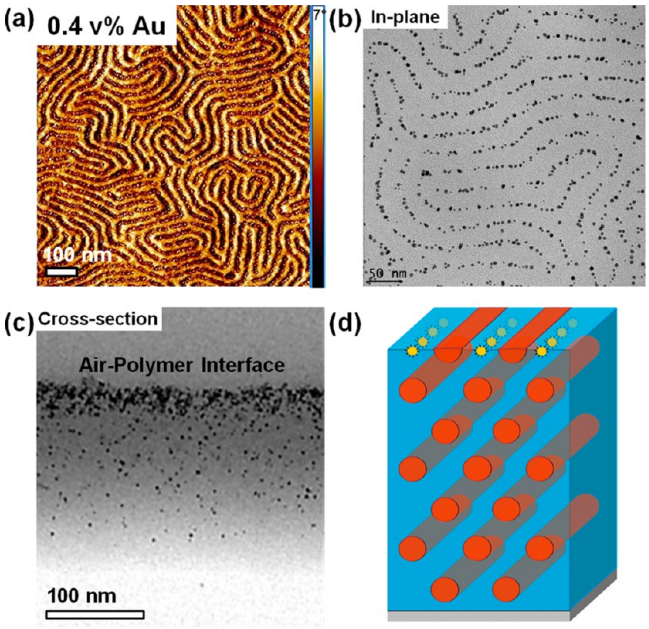

Figure 1. (a) AFM (phase), (b) top-view TEM, and (c) cross-sectional TEM images of a ~200 nm supramolecular nanocomposite thin film containing PS(19 kDa)-*b*-P4VP(5.2 kDa)$(PDP)_{1.7}$ and only 0.4 vol % of Au NPs. The NPs mainly segregated to the P4VP$(PDP)_{1.7}$ microdomains at air/film interface as illustrated in (d).

As ϕ_{NP} increases to 0.7 vol %, there is an extra 1D NP chain in the middle of every two NP chains in the fingerprint patterns in some areas (Figure 2a). When ϕ_{NP} reaches 1.5 vol %, the morphology of the film becomes homogeneous across the surface (Figure 2b). The cross-sectional TEM image indicates that the darker/denser NP chain in the top-view TEM image originates from the projection of the NP chains residing in the first, third, and fifth layers of interstitial sites from the surface and the lighter-colored region is from the NP chains in the interstitial sites in the second and fourth layers (Figure 2b). At ϕ_{NP} = 2.9 vol %, the NPs occupy all 10 layers of the interstitial sites throughout the entire film thickness, resulting in a 3D NP array consisting of hexagonally packed single NP chains (Figure 2c).

The morphology of each supramolecular nanocomposite thin film is also characterized using grazing incidence small-angle X-ray scattering (GISAXS) at an incident angle larger than the critical angle, α, of the film (Figure 3). To the first approximation, when there is a periodic structure in the lateral direction with average spacing a in the film, the Bragg's law can be satisfied, leading to a strong Bragg peak at $q_y = 2\pi/a$ in the 2D GISAXS pattern. Here, Bragg rods at q_y = 0.0192 $Å^{-1}$ corresponding to the lateral periodicity of the NP chains can be clearly seen when ϕ_{NP} = 0.5 vol % (Figure 3a). However, no oscillatory feature is observed on the Bragg rods in the q_z direction, agreeing with the TEM results that the NPs arrays mainly locate on the film surface. When ϕ_{NP} reaches 1.5 vol %, strong diffraction spots corresponding to the hexagonally packed in-plane NP arrays are clearly seen on the first and second order Bragg peaks and can be attributed to the 3D NP assembly near the air/film interface (Figure 3b).[42] The intensity of the Bragg spots become stronger and higher order peaks appear in the q_z direction as ϕ_{NP} increases to 2.9 vol % (Figure 3c). This indicates that more layers of hexagonally packed NP chains are present in the interior of the film as a result of the propagation of the surface-directed NP assembly throughout the entire film thickness.[42] Within the experimental error introduced during the solvent annealing process, the lateral periodicities of the nanocomposite thin films in Regime I remain around 33 nm.

The surface-directed nanoparticle assembly in Regime I is observed as a result of the interplay of thermodynamics and assembly kinetics. Thermodynamically, the favorable alkyl ligand-P4VP(PDP) interactions, $\Delta H_{ligand/polymer}$, and the entropic gain in the conformational entropy, S_{con}, drive the Au NPs into the middle of the P4VP$(PDP)_{1.7}$ domains upon NP incorporation. In addition, the low surface tension of the NP ligand (25 mN/m), which is smaller than that of PS (33 mN/m), P4VP (42 mN/m), and PDP (27 mN/m), directs the NPs to migrate to the top of the P4VP$(PDP)_{1.7}$ half cylinders to lower the surface energy, $\Delta H_{surface}$, of the film after solvent annealing. This leads to a 1D NP chain with well-defined interparticle distance in each P4VP$(PDP)_{1.7}$ near the air/film interface. As the ϕ_{NP} increases, the NPs segregate to the closest interstitial sites among cylindrical domains to maximize entropic gain in ΔS_{con} and the energetic gain in $\Delta H_{ligand/polymer}$.

Kinetically, the vertical solvent field generated during spin-casting may not only lead to microdomains oriented perpendicular to the surface, but also a concentration gradient of the NPs in the film when ϕ_{NP} < 1.5 vol %. As the solvent diffuses into the film, the microdomains reorient from perpendicular to parallel orientation starting from the air/film interface.[43] The NPs near the surface undergo short-range diffusion and segregate to the closest interstitial sites in the first few layers to reach a local energy minimum. This results in the surface-directed NP assembly observed at ϕ_{NP} < 1.5 vol %. When ϕ_{NP} reaches 2.9 vol %, there are sufficient NPs that pack densely in all the P4VP$(PDP)_{1.7}$ domains throughout the entire film thickness after spin-casting. As the nanocomposite orders during solvent annealing, every interstitial site becomes

DOI: 10.1021/jacs.5b02494
J. Am. Chem. Soc. 2015, 137, 6356−6365

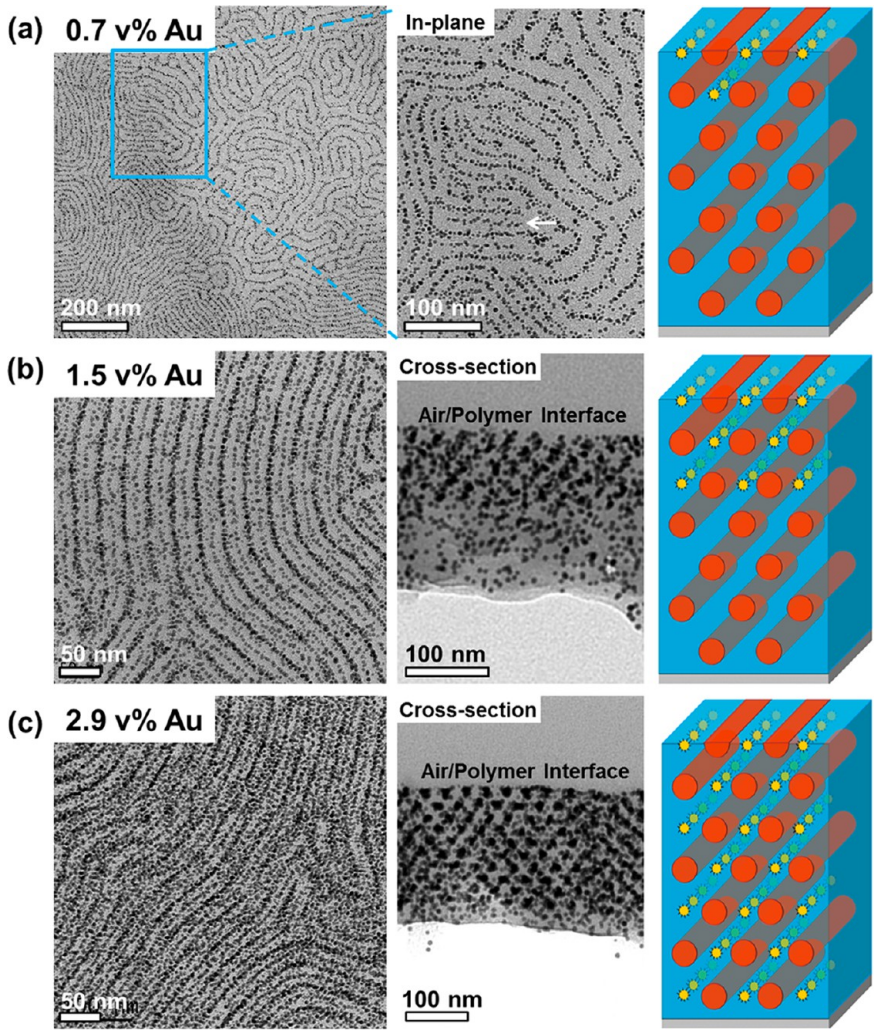

Figure 2. Top-view and cross-sectional TEM images of ~200 nm supramolecular nanocomposite thin films containing PS(19 kDa)-*b*-P4VP(5.2 kDa)$(PDP)_{1.7}$ and (a) 0.7, (b) 1.5, and 2.9 vol % of Au NPs. The surface energy plays an important role in the NP assembly, driving the NPs to segregate to the P4VP$(PDP)_{1.7}$ domains starting from the interstitial sites at the surface. The surface-directed assembly then propagates into the film as ϕ_{NP} increases. The morphology of the nanocomposite becomes homogeneous at ϕ_{NP} = 2.9 vol % when the hexagonally packed in-plane NP chains are observed in the interstitial sites throughout the entire film thickness.

occupied by the NPs in the vicinity, leading to hexagonally packed in-plane NP chains with homogeneous NP concentration in the interior of the film.

Regime II: 3 vol % < ϕ_{NP} < 15 vol %. The AFM and cross-sectional TEM images of ~200 nm thin films at ϕ_{NP} = 4.4 and 7.3 vol % are shown in Figure 4a,b, respectively. The AFM images confirm that both films have in-plane cylindrical morphology. When ϕ_{NP} = 4.4 vol %, the majority of the NPs still reside in the interstitial sites (Figure 4a) and there are some NPs dispersed in the P4VP$(PDP)_{1.7}$ matrix as illustrated in Figure 4a. As ϕ_{NP} reaches 7.3 vol %, the NPs become homogeneously dispersed in the matrix, resulting in 3D NP networks throughout the entire film thickness (Figure 4b). In the GISAXS pattern, the Bragg spots corresponding to the in-plane hexagonal morphology can be observed for both films (Figure 5). In addition, the q_y scan of the two GISAXS patterns reveals a shift of the first order Bragg peak to higher q values as ϕ_{NP} increases. Interestingly, the lateral periodicities of the nanocomposites with 4.4 and 7.3 vol % of NPs drop to 31.8 and 29.6 nm, respectively.

In Regime II, the interstitial sites are fully occupied. Accommodating more NPs into the interstitial regions is entropically unfavorable. Hence, the NPs begin to disperse within the P4VP$(PDP)_{1.7}$ matrix, which leads to an enthalpic gain in $\Delta H_{ligand/polymer}$ and an entropic gain in translational entropy, S_{trans}, due to the new configurations of the NP arrangements in the system. During solvent annealing, the solvent molecules effectively modify the conformation of the P4VP$(PDP)_{1.7}$ chains and reduce its rigidity, lowering the activation energy barrier for the NPs to diffuse into the middle of the P4VP$(PDP)_{1.7}$ matrix to form interconnected 3D NP networks in the films. Moreover, when the P4VP$(PDP)_{1.7}$ chains become less rigid, some NPs may enter the comb blocks. This disrupts the molecular packing of the PDP small molecules in the domains, leading to a decrease in the periodicity of the supramolecular nanocomposite.[44]

Regime III: 15 vol % < ϕ_{NP} < 20 vol %, Kinetically-Trapped Nanoparticle Assembly. Drastic change of the orientation of the NP arrays and the microdomains is observed when ϕ_{NP} reaches 14.7 vol %. The AFM image of the film surface shows hexagonally packed cylindrical domains,

DOI: 10.1021/jacs.5b02494
J. Am. Chem. Soc. 2015, 137, 6356−6365

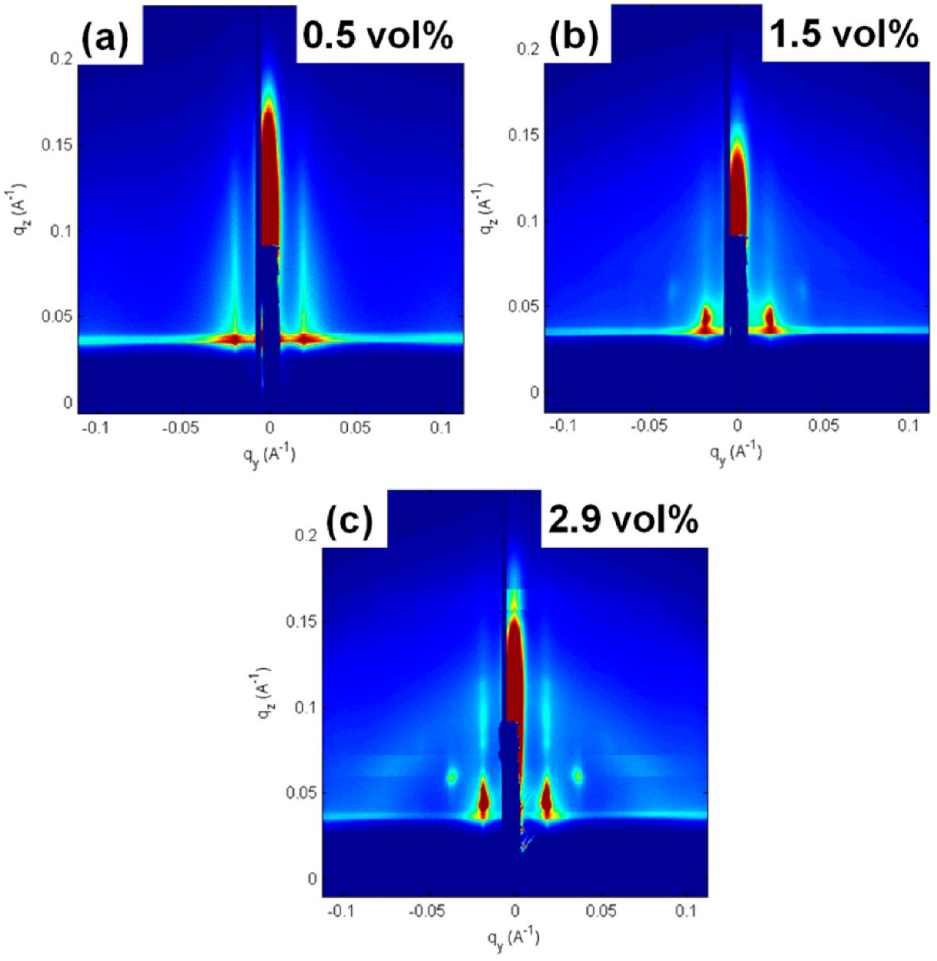

Figure 3. GISAXS patterns of the ~200 nm supramolecular nanocomposite thin films containing PS(19 kDa)-*b*-P4VP(5.2 kDa)$(PDP)_{1.7}$ and (a) 0.5, (b) 1.5, and (c) 2.9 vol % of ~4.9 nm Au NPs, respectively. All three GISAXS patterns were taken at $\alpha = 0.22°$, which is larger than the critical angles of the films. The intensity of the Bragg spots corresponding to the hexagonally packed NP chains becomes stronger and higher order peaks appear in the q_z direction as ϕ_{NP} increases. This indicates an increase of the number of layers of the ordered 3D NP array in the films as a function of ϕ_{NP}. The q_y position of the 1st order Bragg peak remains at similar positions as ϕ_{NP} increases from 0 to 2.9 vol %, corresponding to a lateral periodicity ~33 nm.

presumably to be the perpendicularly oriented PS cylinders surrounded by the NPs dispersed in the P4VP(PDP) matrix (Figure 6a). The NPs in the P4VP$(PDP)_{1.7}$ matrix form honeycomb-like assemblies (Figure 6b). The cross-sectional TEM image further reveals that the NP arrays prevail throughout the entire film thickness but are not perfectly aligned normal to the surface. Figure 6c shows that the perpendicular cylindrical domains assume a finite distribution of tilt angles with respect to the air/film interface. The strong Bragg rods in the q_y direction in the GISAXS pattern in Figure 6d confirm the overall perpendicular orientation of the morphology in the film as illustrated in Figure 6e. On the basis of the q_y linecut of the 2D GISAXS pattern, the lateral periodicity further decreases to 27.1 nm at ϕ_{NP} = 14.7 vol %.

When the supramolecular nanocomposite thin film is in Regime III, the P4VP$(PDP)_{1.7}$ domains are highly loaded with NPs, resulting in a long-lived nonequilibrium structure. During spin-casting, the vertical solvent field biases the supramolecular microdomains to orient perpendicular to the surface.[45] The coalescence of neighboring cylinders leads to a poorly ordered perpendicular morphology in the as-cast film. At low NP loadings, solvent annealing provides sufficient mobility that allows the supramolecular nanocomposite to overcome the activation energy barrier to escape the kinetically trapped state and form ordered parallel morphology. At high ϕ_{NP}, however, the NPs occupy the majority space in P4VP$(PDP)_{1.7}$ microdomains and some NPs may even locate near the interface between the two blocks after spin-casting. The hard framework set up by the NPs in the P4VP$(PDP)_{1.7}$ domains pins down the supramolecules, increases the activation energy barrier for interdomain diffusion, and hinders the long-range diffusion. This discourages the reorientation of the microdomains from perpendicular to ordered parallel morphology during solvent annealing. Hence, the nanocomposite thin film becomes kinetically arrested in the long-lived nonequilibrium morphology generated during spin-casting and the morphology remains the same even after prolonged solvent annealing.

Regime IV: 20 vol % < ϕ_{NP} < 30 vol %, Macrophase Separation of Nanoparticles. With 14.7 vol % of NPs in the P4VP$(PDP)_{1.7}$ domains, the total volume fraction of the matrix becomes 77 vol % since the volume fraction of the comb block is 62 vol % in PS(19 kDa)-*b*-P4VP(5.2 kDa)$(PDP)_{1.7}$. In bulk, the supramolecules form spherical morphology when f_{comb} reaches above 82 vol %.[46] To investigate if the supramolecular nanocomposite undergoes morphological transition at high ϕ_{NP} and to test the thermodynamic limit of ϕ_{NP} in the film, we

DOI: 10.1021/jacs.5b02494
J. Am. Chem. Soc. 2015, 137, 6356−6365

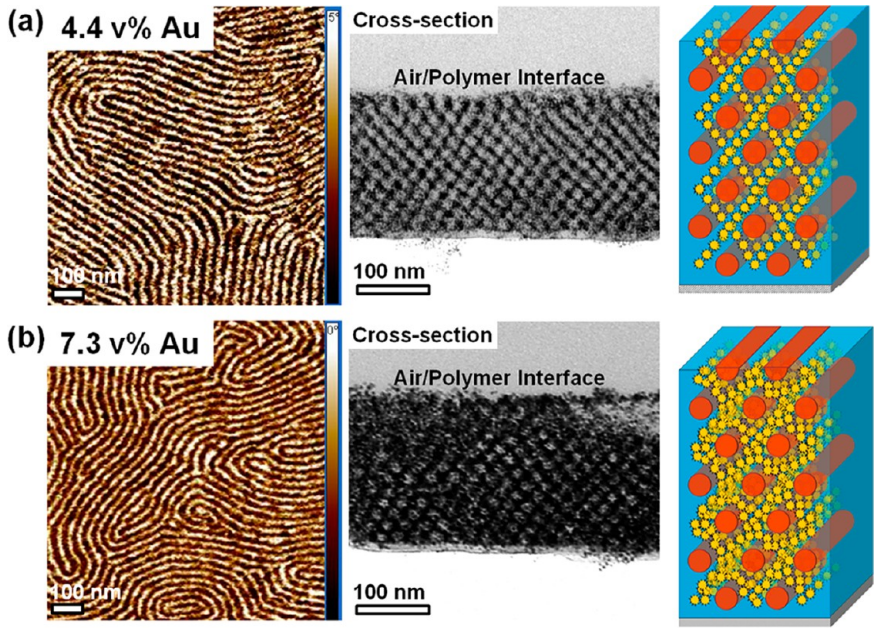

Figure 4. AFM (phase) and cross-sectional TEM images of ~200 nm supramolecular nanocomposite thin films containing PS(19 kDa)-*b*-P4VP(5.2 kDa)$(PDP)_{1.7}$ and (a) 4.4 and 7.3 vol % of ~4.9 nm Au NPs. The NPs are driven to the interstitial sites as well as the P4VP$(PDP)_{1.7}$ matrix by $\Delta H_{ligand/polymer}$ and ΔS_{trans}, leading to 3D NP networks in the interior of the films.

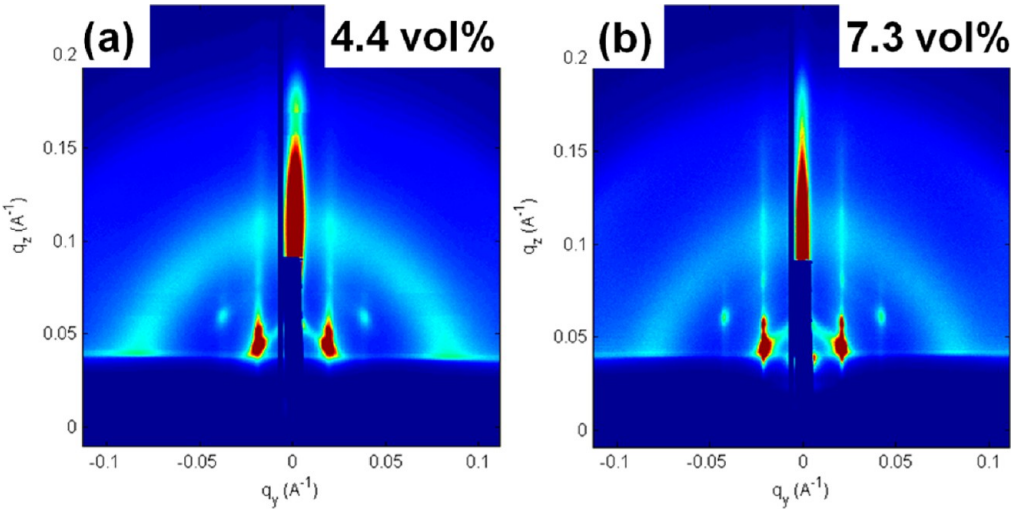

Figure 5. Parts (a) and (b) show the GISAXS patterns of the ~200 nm supramolecular nanocomposite thin films containing 4.4 and 7.3 vol % of ~4.9 nm Au NPs, respectively. The Bragg spots at high q_z suggest the presence of the 3D NP structure in both films. The shift of the 1st order Bragg peak to high q_y values indicates a decrease of the lateral periodicity from 31.8 to 29.6 nm as ϕ_{NP} increases from 4.4 to 7.3 vol %. The GISAXS patterns were taken at α = 0.22° and 0.23°, respectively.

further increase ϕ_{NP} to >22 vol %. Figure 7a shows the AFM of a ~200 nm PS(19 kDa)-*b*-P4VP(5.2 kDa)$(PDP)_{1.7}$ supramolecular nanocomposite thin film containing 22.0 vol % of ~4.9 nm Au NPs. The upper half and the bottom half of the AFM image, which are separated by a blue dashed line, show the surface morphology of the film under a weaker and a stronger tapping force, respectively. When the tapping force is small, NP assemblies can be observed whereas the feature of the microphase-separated cylindrical morphology is only seen when the tapping force is large (Figure 7a). As ϕ_{NP} increases to 29.3 vol %, the AFM image only shows NP assemblies on the film surface regardless of the tapping force (Figure 7b).

The GISAXS pattern of the sample containing 22.0 vol % of NPs shows the Bragg peak corresponding to the perpendicular cylindrical morphology with a lateral periodicity only ~26 nm (Figure 8a). Interestingly, two peaks representing interparticle distances ~5.6 and ~5.0 nm are present on the q_y linecut (Figure 8a and 8c). Similar results are observed in the GISAXS pattern of the sample with 29.3 vol % of NPs as shown in Figure 8b and 8c. To further characterize the internal structure of the film, GISAXS was conducted on both samples at different incident angles (α) (see SI-3). When α is smaller than the critical angle of the film (α = 0.15°), the peak corresponding to a ~5.6 nm interparticle distance has a relatively higher intensity than that for the smaller interparticle distance (~5.0 nm). As α increases, the intensity of the peak decreases and the Bragg peaks corresponding to the lateral periodicity of the nanocomposite and the interparticle distance

DOI: 10.1021/jacs.5b02494
J. Am. Chem. Soc. 2015, 137, 6356−6365

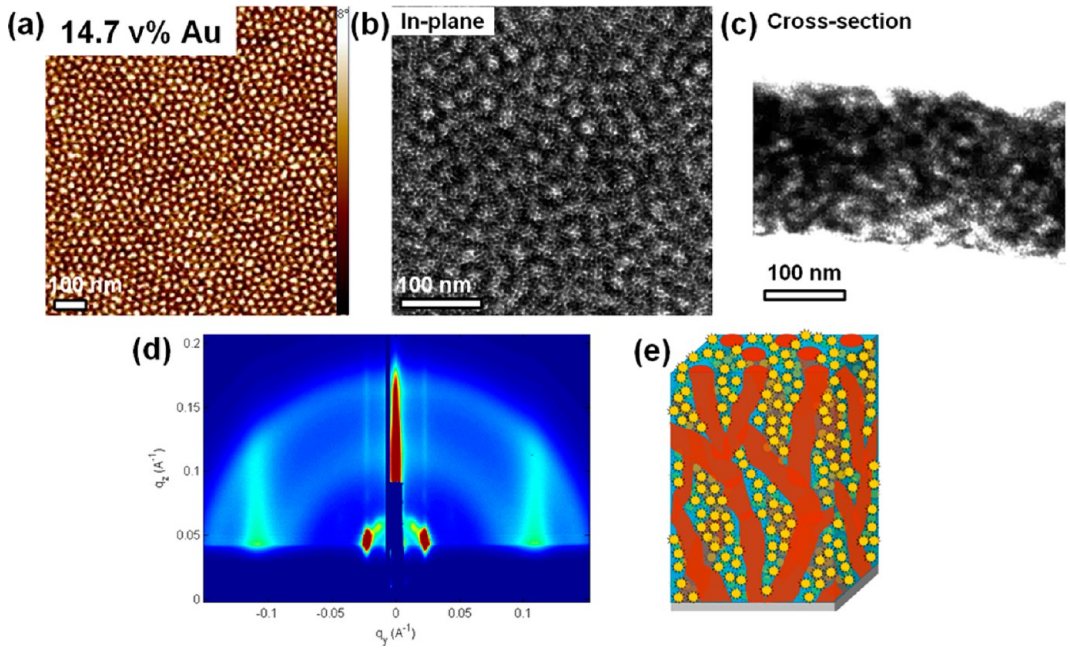

Figure 6. (a) AFM (phase), (b) top-view TEM, (c) cross-sectional TEM images, and (d) GISAXS pattern (α = 0.24°) of a ∼200 nm supramolecular nanocomposite thin film containing PS(19 kDa)-*b*-P4VP(5.2 kDa)$(PDP)_{1.7}$ and 14.7 vol % of ∼4.9 nm Au NPs. Jamming of NPs in the interior of the film leads to a long-lived kinetically trapped perpendicular cylindrical morphology with a lateral periodicity around 27.1 nm in the nanocomposite. The strong Bragg rods in the q_y direction confirm the overall perpendicular orientation of the morphology in the film as illustrated in (e).

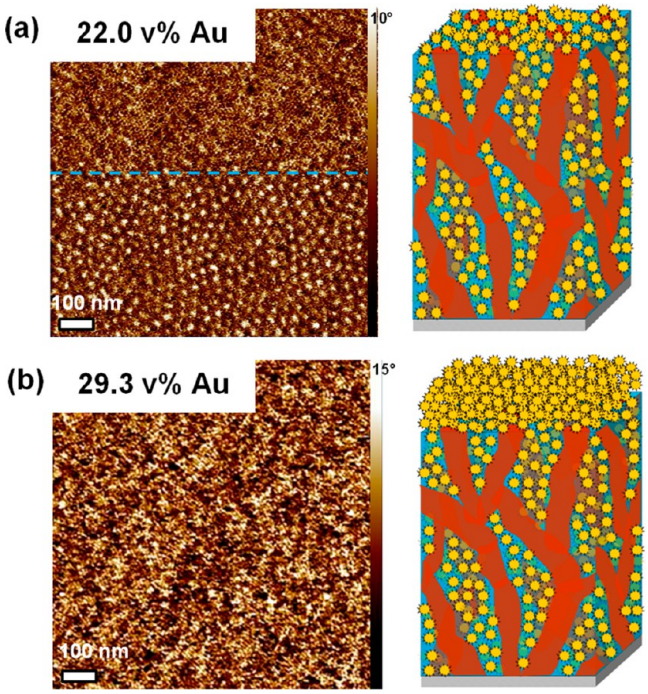

Figure 7. AFM images (phase) of the ∼200 nm PS(19 kDa)-*b*-P4VP(5.2 kDa)$(PDP)_{1.7}$ supramolecular thin films containing (a) 22.0 and (b) 29.3 vol % of ∼4.9 nm Au NPs. At ϕ_{NP} = 22.0 vol %, some NPs form a monolayer of NP assemblies at the air/film interface. The film surface becomes completely covered by multiple NP layers at ϕ_{NP} = 29.3 vol % as no microphase-separated nanostructure can be observed in the AFM image in (b).

∼5.0 nm become stronger. This indicates that the NPs near the film surface have an average interparticle distance ∼5.6 nm, which is slightly larger than that of the NPs coassembled with the supramolecules in the film.

In Regime IV, the volume fraction of the $P4VP(PDP)_{1.7}$ domains reaches 84.0 vol % at ϕ_{NP} = 22 vol %, indicating that the original cylindrical supramolecular nanocomposite is in the spherical morphology regime. However, the results show no sign of cylinder-to-sphere order−order transition in the film. Usually, the increase in the effective volume of the matrix may bend the interface and the NPs may stabilize the curvature of the spheres to induce morphological transition. However, in our case, the threshold ϕ_{NP} for cylinder-to-sphere order−order transition is above the critical NP fraction to be soluble in the supramolecular structure. Between 14.7 and 22.0 vol %, the nanocomposite possibly reaches a ϕ_{NP} limit at which it becomes too energetically costly to deform the polymer chains to accommodate more NPs in $P4VP(PDP)_{1.7}$ domains. Therefore, ΔS_{con} can easily offset $\Delta H_{ligand/polymer}$, which only relies on weak van der Waals interactions. In addition, as more and more NPs get close to the PS/$P4VP(PDP)_{1.7}$ interface, more energy loss needs to be compromised due to the unfavorable ligand/PS enthalpic interactions. These thermodynamic driving forces expel the excess amount of NPs from the interior of the film to the air/film interface. In addition, at high NP loadings, the film surface may be covered by the 1-dodecanethiol free ligands, which mediate the unfavorable interactions between the PS cylinders and the NPs at the air/film interface. This promotes the formation of the NP assemblies on the surface to maximize the energetic gains in $\Delta H_{surface}$ and the particle−particle interactions, which further induces a growth of the NP assemblies on the surface of the film as ϕ_{NP} increases. Decreasing NP size and enhancing $\Delta H_{ligand/polymer}$ via hydrogen bonding or ionic interactions may suppress ΔS_{con} and allow higher NP loadings to be

DOI: 10.1021/jacs.5b02494
J. Am. Chem. Soc. 2015, 137, 6356−6365

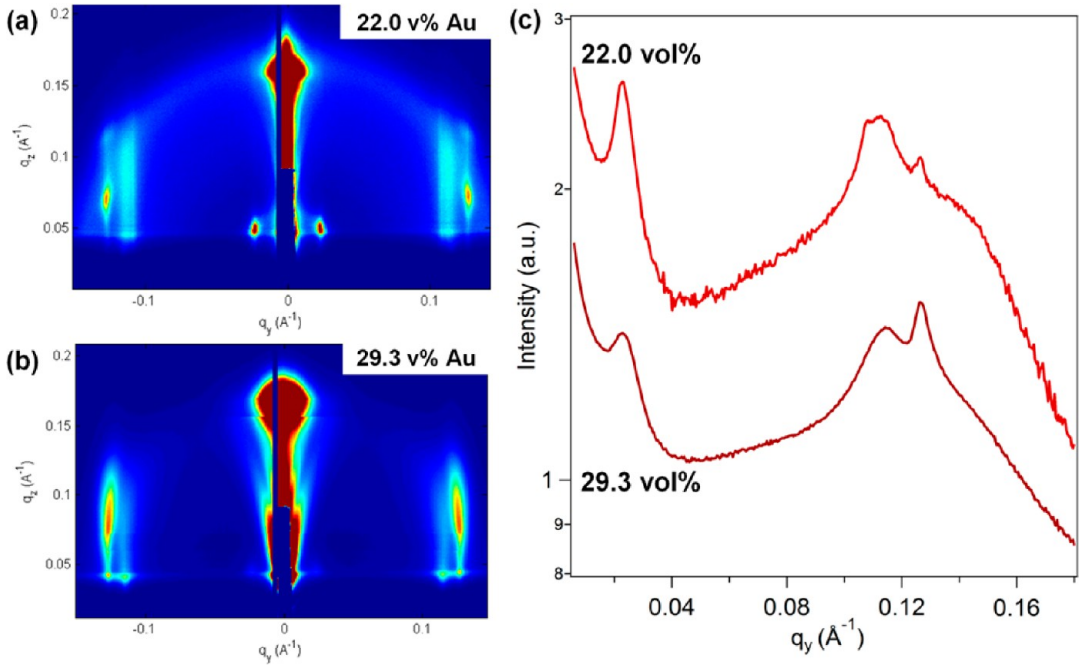

Figure 8. (a) and (b) show the GISAXS patterns of the ~200 nm supramolecular nanocomposite thin films containing 22.0 and 29.3 vol % of the 4.9 nm Au nanoparticles taken at $\alpha = 0.27°$ and 0.29°, respectively. (c) shows the q_y lincuts of the GISAXS patterns shown in (a) and (b) at $q_z = 0.04$ Å^{-1}. The 1st order Bragg peak seen at high α corresponds to the microphase-separated supramolecule framework and shifts to higher q_y values as ϕ_{NP} increases, indicating a decrease of the lateral periodicity of the supramolecular nanocomposite from 26.5 to 26 nm as ϕ_{NP} increases from 22.0 to 29.3 vol %.

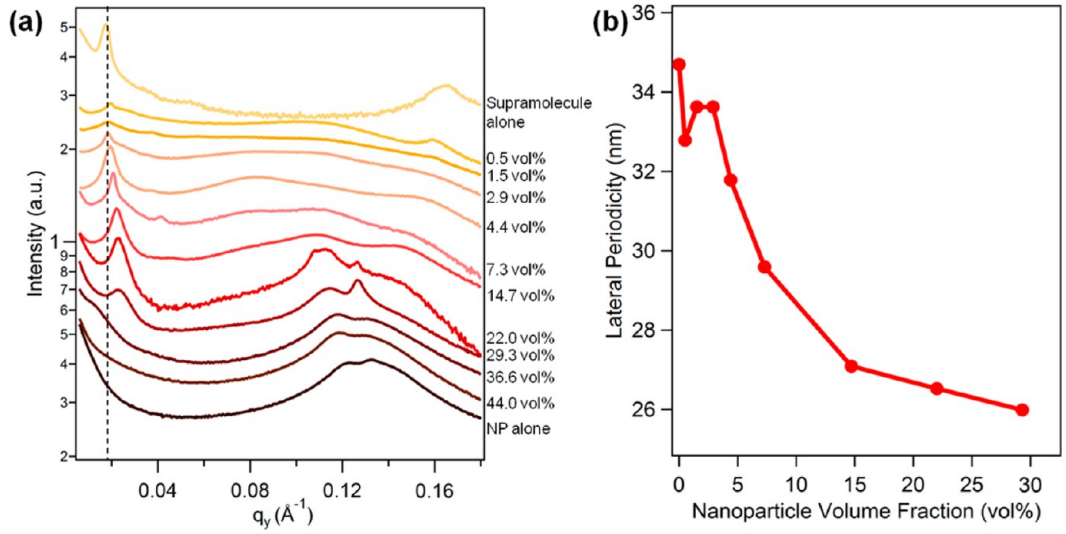

Figure 9. (a) q_y linecuts of the GISAXS patterns at $q_z = 0.04$ Å^{-1} for the ~200 nm PS(19 kDa)-*b*-P4VP(5.2 kDa)$(PDP)_{1.7}$ supramolecular nanocomposite thin films with different ϕ_{NP}. The 1st order Bragg peak shifts to higher q_y values as ϕ_{NP} increases, corresponding to a decrease of the lateral periodicity of the supramolecular nanocomposite with increasing ϕ_{NP} as summarizes in (b). At high NP loadings, the NPs may occupy the P4VP$(PDP)_{1.7}$ domain and disrupt the packing of the comb blocks, altering the hierarchical structure of the comb blocks and leading to a decrease of the lateral periodicity of the nanostructure.

incorporated in the film, which requires further investigation in the future.

In Regime V (ϕ_{NP} > 30 vol %), preliminary AFM and GISAXS results demonstrate that the NPs dominate the assembly and form 3D NP lattices in the film (see SI-4). No microphase-separated nanostructure is observed and the supramolecules seem to be dispersed in the NP lattices. More in-depth study is required to understand the spatial distribution of the supramolecules in the film at high ϕ_{NP}.

Lastly, the lateral periodicity of the nanocomposite decreases as a function of ϕ_{NP} as evidenced by the q_y linecuts of all the GISAXS patterns (Figure 9). When ϕ_{NP} is low (ϕ_{NP} > 3 vol %), the average lateral periodicity remains ~33 nm. The small deviation of the spacing from the average value is mainly due to the experimental differences in the solvent annealing and solvent evaporation conditions. At high ϕ_{NP}, some of the NPs may enter the comb blocks, disrupting the crystallization of the small lamellae in the P4VP$(PDP)_{1.7}$ domains during spin-

DOI: 10.1021/jacs.5b02494
J. Am. Chem. Soc. 2015, 137, 6356−6365

casting as schematically depicted in Figure 10.[46,47] This conformational change of the chain architecture is not

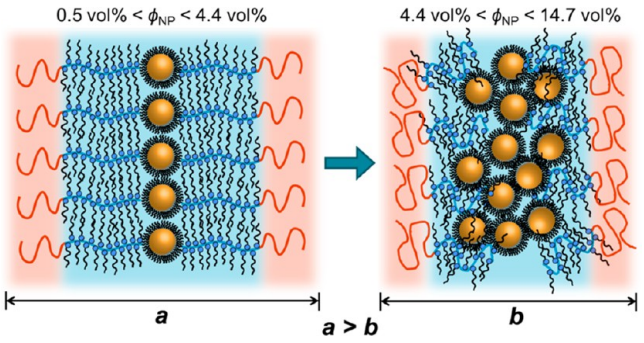

Figure 10. Schematic drawings of the chain conformations of PS and P4VP(PDP)$_{1.7}$ chains and the spatial distribution of NPs at relatively low and high NP loadings. When ϕ_{NP} is high, the NPs in the P4VP(PDP)$_{1.7}$ domains may get into the comb blocks and disrupt the crystallization of the small lamellae. This leads to a bottlebrush-like architecture of the P4VP(PDP)$_{1.7}$ chains and a change of the PS conformation to accommodate the cross-sectional mismatch at the interface between the two blocks. The lateral periodicity of the microdomains, therefore, may decrease as a result of the altered chain architecture of the supramolecules at high ϕ_{NP}.

alleviated when the solvent enters the film during solvent annealing. During solvent annealing, the solvent molecules further disrupt the hierarchical structure in the P4VP(PDP)$_{1.7}$ domains, allowing more NPs to diffuse into the comb blocks. As a result, the P4VP(PDP)$_{1.7}$ chains no longer have comb-like architectures and may assume bottlebrush-like conformations (Figure 10). This induces a larger cross-sectional mismatch at the interface between the two blocks than that in a coil-comb supramolecule framework. The PS chains need to change their conformations near the interface to accommodate the change in the cross-sectional area at the interface, which also leads to a decrease in their end-to-end distance in the lateral direction (Figure 10). Unlike those in highly loaded supramolecular nanocomposites, the NPs in the films with relatively small ϕ_{NP} locate in the middle of the P4VP(PDP)$_{1.7}$ domains, leaving semicrystalline comb blocks with larger contour lengths.[46,47] Thus, the lateral periodicity in the supramolecular nanocomposites with low ϕ_{NP} (a) is larger than that with high ϕ_{NP} (b) as shown in Figure 10.

CONCLUSIONS

In summary, the phase behavior of supramolecular nanocomposite thin films was systematically investigated as a function of NP loading. The complicated interplay between the thermodynamic and kinetic considerations significantly influences the morphology of the nanocomposites in different ϕ_{NP} regimes, resulting in various multidimensional hierarchical NP assemblies in the system (Figure 11). In cylindrical supramolecular nanocomposite thin films, a delicate balance among $\Delta H_{surface}$, ΔS_{con}, and $\Delta H_{ligand/polymer}$ drive the surface-directed NP assembly in Regime I (ϕ_{NP} < 3 vol %). The NPs occupy the first few layers of interstitial regions in the cylindrical morphology starting from the ones at the surface as NP loading increases. In Regime II (3 vol % < ϕ_{NP} < 15 vol %), ΔS_{trans} and $\Delta H_{ligand/polymer}$ offset ΔS_{con}, leading to NP assemblies in not only the interstitial sites, but also the 3D NP networks in the P4VP(PDP) matrix throughout the entire film thickness. When the thermodynamic limit of ϕ_{NP} is reached in Regime III (15 vol % < ϕ_{NP} < 20 vol %), kinetically trapped perpendicular morphology is observed in the nanocomposite. As ϕ_{NP} reaches Regime IV (20 vol % < ϕ_{NP} < 30 vol %), no NP induced cylinder-to-sphere morphological transition is observed as the NPs begin to macrophase separate to form NP assemblies on top of the film. Eventually, the coassembly breaks down as the NPs dominate the assembly in the system at high ϕ_{NP} (Regime V). The supramolecular approach can be used to generate thin films with not only 1D/2D NP assemblies with single particle precision, but also in-plane/out-of-plane 3D NP assemblies with high NP volume fraction, i.e., > 50 wt %, over large areas. This opens a new avenue to fabricate functional nanocomposite thin films for the realization of a wide range of applications such as optical coatings, plasmon-enhanced photovoltaics, high-energy-density thin film capacitors, and catalysis.

EXPERIMENTAL SECTION

Sample Preparation. PS(19 000)-*b*-P4VP(5200) (PDI = 1.09) was purchased from Polymer Source, Inc. 3-*n*-Pentadecylphenol (95%) was purchased from Acros. Chloroform was purchased from Fisher. The ~4.9 nm gold nanoparticles were synthesized following a previously reported method.[48] All the reagents for gold nanoparticle synthesis were purchased from Sigma-Aldrich. All chemicals were used as received. Blends of supramolecules and nanoparticles were prepared as described previously.[42] Thin films were prepared by spin-coating the mixed solutions onto silicon wafers at spinning speeds ranging from

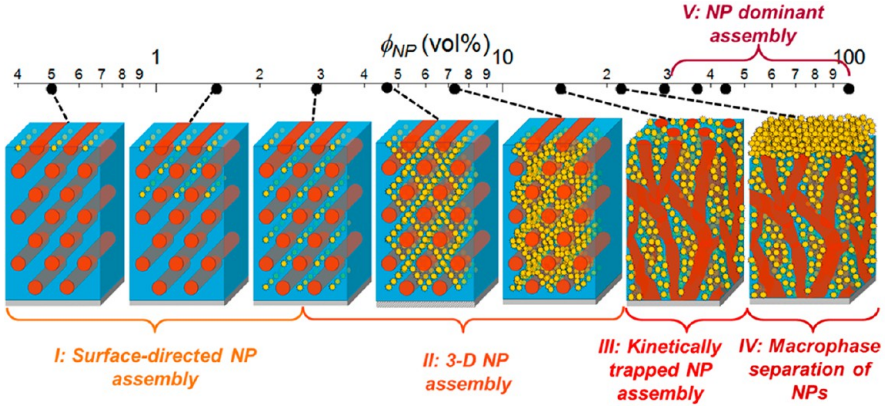

Figure 11. Summary of the morphologies in the supramolecular nanocomposite thin films with different NP volume fractions ranging from 0.4 to 45 vol %.

DOI: 10.1021/jacs.5b02494
J. Am. Chem. Soc. 2015, 137, 6356−6365

1000 to 3000 rpm. Sample thicknesses were measured using a Filmetrics F20 interferometer. When preparing the supramolecular nanocomposite thin films with high nanoparticle volume fractions, some solvent was dried from the nanocomposite solutions and the spin-casting speed was decreased to 800 rpm to generate ∼200 nm nanocomposite thin films. For solvent annealing, samples with ϕ_{NP} < 10 vol % were annealed using 300 μL of $CHCl_3$ injected inside a 250 mL top-capped jar at 22.5 °C. Once the film thickness of the nanocomposite thin film reached 145−150% of its original thickness, the jar was opened and the $CHCl_3$ vapor inside the jar was allowed to freely evaporate.[43] The same solvent annealing condition, i.e. fixed annealing time and amount of $CHCl_3$ used, was used to anneal the films with ϕ_{NP} > 10 vol %. We observed that the morphology of the highly loaded nanocomposite thin films remains the same as the annealing time and solvent vapor pressure increases.

Atomic Force Microscopy. AFM was performed on a Veeco Dimension 3100 with a Nanoscope III controller and a Quadrex extension box. The spring constant of the cantilever was 10−130 N m^{-1} with a resonant frequency in the range of 300−500 kHz. The set point for auto tune was ∼1.5 V. The set-point amplitude was 90% of the free vibration value.

Grazing Incidence Small-Angle X-ray Scattering. GISAXS experimental measurements were made at beamline 7.3.3 at the ALS in Lawrence Berkeley National Laboratory and at beamline 8-ID-E the APS in Argonne National Laboratory. X-ray wavelengths of 1.687 and 1.240 Å were used at APS, and ALS, respectively. The scattering intensity distribution was captured by a Pilatus 1 M detector at ALS and APS. The intensities (I) are plotted with respect to q, where $q = (4\pi/\lambda)\sin(\theta/2)$, λ is the wavelength of the incident X-ray beam, and θ is the scattering angle.

Transmission Electron Microscopy. PS-*b*-P4VP(PDP)$_r$ thin films were spun cast on polystyrene-coated sodium chloride (NaCl) disks in a manner similar to those on silicon substrates. After solvent annealing, films were floated off the substrate onto the surface of a water pool. Thin films were retrieved with carbon film coated copper grids. The top-view TEM images were collected on a FEI Tecnai 12 transmission electron microscope at an accelerating voltage of 120 kV. To prepare the cross-section of a nanocomposite thin film, the sample was first prepared on NaCl disk. Then, the thin film was floated off from the substrate on the surface of a water pool. An epoxy block (Araldite 502, Electron Microscopy Sciences) was used to catch the film such that the sample is on top of the epoxy block with the air−polymer interface in contact with the top of the epoxy block. The epoxy along with the sample were cured at 60 °C for at least 4 h to ensure good contact between the epoxy and the nanocomposite thin film. Thin sections, ∼60 nm in thickness, were microtomed using an RMC MT-X Ultramicrotome (Boeckler Instruments) and picked up on copper TEM grids. The cross-sectional TEM images were collected using a FEI Tecnai 12 transmission electron microscope at an accelerating voltage of 120 kV.

Thermogramimetric Analysis. TGA was performed on a TGA 500 thermogravimetric analyzer heating at a rate of 10 °C/min from room temperature to 550 °C under a continuous purge of nitrogen.

■ ASSOCIATED CONTENT

Supporting Information

Size analysis of the gold nanoparticles used in this study, the method used to calculate ϕ_{NP} in the supramolecular nanocomposite thin films, the discussion on the interparticle distances in the supramolecular nanocomposite thin films in Regime IV (20 vol % < ϕ_{NP} < 30 vol %), and the discussion on the morphologies of the supramolecular nanocomposite thin films in Regime V (ϕ_{NP} > 30 vol %). The Supporting Information is available free of charge on the ACS Publications website at DOI: 10.1021/jacs.5b02494.

■ AUTHOR INFORMATION

Corresponding Author

*tingxu@berkeley.edu

Notes

The authors declare no competing financial interest.

■ ACKNOWLEDGMENTS

The authors thank Dr. Zhang Jiang and Dr. Joseph Strzalka at beamline 8-ID-E in Advanced Photon Source and the staff at beamline 7.3.3 in Advanced Light Source for their inputs and help on the GISAXS studies. This work was supported by the Department of Energy, Office of Basic Energy Science under Contract DE-AC02-05CH11231 through the "Organic−Inorganic Nanocomposites" program at Lawrence Berkeley National Laboratory (J.K. and T.X.). Use of the Advanced Photon Source was supported by the U.S. Department of Energy, Office of Science, Office of Basic Energy Sciences, under contract DE-AC02-06CH1135.

■ REFERENCES

(1) Balazs, A. C.; Emrick, T.; Russell, T. P. *Science* **2006**, *314* (5802), 1107−1110.
(2) Bockstaller, M. R.; Mickiewicz, R. A.; Thomas, E. L. *Adv. Mater.* **2005**, *17* (11), 1331−1349.
(3) Millo, O.; Azulay, D.; Toker, D.; Balberg, I. *Int. J. Mod. Phys. A* **2004**, *18* (15), 2091−2121.
(4) Grimaldi, C.; Balberg, I. *Phys. Rev. Lett.* **2006**, *96* (6), 066602.
(5) Sankaran, V.; Cummins, C. C.; Schrock, R. R.; Cohen, R. E.; Silbey, R. J. *J. Am. Chem. Soc.* **1990**, *112* (19), 6858−6859.
(6) Chan, Y. N. C.; Craig, G. S. W.; Schrock, R. R.; Cohen, R. E. *Chem. Mater.* **1992**, *4* (4), 885−894.
(7) Chan, Y. N. C.; Schrock, R. R.; Cohen, R. E. *Chem. Mater.* **1992**, *4* (1), 24−27.
(8) Templin, M.; Franck, A.; Du Chesne, A.; Leist, H.; Zhang, Y.; Ulrich, R.; Schädler, V.; Wiesner, U. *Science* **1997**, *278* (5344), 1795−1798.
(9) Du, P.; Li, M.; Douki, K.; Li, X.; Garcia, C. B. W.; Jain, A.; Smilgies, D. M.; Fetters, L. J.; Gruner, S. M.; Wiesner, U.; Ober, C. K. *Adv. Mater.* **2004**, *16* (12), 953−957.
(10) Kim, S. H.; Misner, M. J.; Yang, L.; Gang, O.; Ocko, B. M.; Russell, T. P. *Macromolecules* **2006**, *39* (24), 8473−8479.
(11) Deshmukh, R. D.; Buxton, G. A.; Clarke, N.; Composto, R. J. *Macromolecules* **2007**, *40* (17), 6316−6324.
(12) Orilall, M. C.; Wiesner, U. *Chem. Soc. Rev.* **2013**, *40* (2), 520−535.
(13) Huh, J.; Ginzburg, V. V.; Balazs, A. C. *Macromolecules* **2000**, *33* (21), 8085−8096.
(14) Thompson, R. B.; Ginzburg, V. V.; Matsen, M. W.; Balazs, A. C. *Science* **2001**, *292* (5526), 2469−2472.
(15) Bockstaller, M. R.; Lapetnikov, Y.; Margel, S.; Thomas, E. L. *J. Am. Chem. Soc.* **2003**, *125* (18), 5276−5277.
(16) Chiu, J. J.; Kim, B. J.; Kramer, E. J.; Pine, D. J. *J. Am. Chem. Soc.* **2005**, *127* (14), 5036−5037.
(17) Lin, Y.; Boker, A.; He, J.; Sill, K.; Xiang, H.; Abetz, C.; Li, X.; Wang, J.; Emrick, T.; Long, S.; Wang, Q.; Balazs, A.; Russell, T. P. *Nature* **2005**, *434* (7029), 55−59.
(18) Li, Q.; He, J.; Glogowski, E.; Li, X.; Wang, J.; Emrick, T.; Russell, T. P. *Adv. Mater.* **2008**, *20* (8), 1462−1466.
(19) Akcora, P.; Liu, H.; Kumar, S. K.; Moll, J.; Li, Y.; Benicewicz, B. C.; Schadler, L. S.; Acehan, D.; Panagiotopoulos, A. Z.; Pryamitsyn, V.; Ganesan, V.; Ilavsky, J.; Thiyagarajan, P.; Colby, R. H.; Douglas, J. F. *Nat. Mater.* **2009**, *8* (4), 354−359.
(20) Zhao, Y.; Thorkelsson, K.; Mastroianni, A. J.; Schilling, T.; Luther, J. M.; Rancatore, B. J.; Matsunaga, K.; Jinnai, H.; Wu, Y.; Poulsen, D.; Frechet, J. M. J.; Alivisatos, A. P.; Xu, T. *Nat. Mater.* **2009**, *8* (12), 979−985.

DOI: 10.1021/jacs.5b02494
J. Am. Chem. Soc. 2015, 137, 6356−6365

(21) Xu, C.; Ohno, K.; Ladmiral, V.; Milkie, D. E.; Kikkawa, J. M.; Composto, R. J. *Macromolecules* **2009**, *42* (4), 1219−1228.
(22) Kim, J.; Green, P. F. *Macromolecules* **2010**, *43* (24), 10452−10456.
(23) Buonsanti, R.; Pick, T. E.; Krins, N.; Richardson, T. J.; Helms, B. A.; Milliron, D. J. *Nano Lett.* **2012**, *12*, 3872−3877.
(24) Colvin, V. L.; Schlamp, M. C.; Alivisatos, A. P. *Nature* **1994**, *370* (6488), 354−357.
(25) Talapin, D. V.; Murray, C. B. *Science* **2005**, *310* (5745), 86−89.
(26) Luther, J. M.; Law, M.; Beard, M. C.; Song, Q.; Reese, M. O.; Ellingson, R. J.; Nozik, A. J. *Nano Lett.* **2008**, *8* (10), 3488−3492.
(27) Kim, D. K.; Lai, Y.; Diroll, B. T.; Murray, C. B.; Kagan, C. R. *Nat. Commun.* **2012**, *3*, 1216.
(28) Scheele, M.; Hanifi, D.; Zherebetskyy, D.; Chourou, S. T.; Axnanda, S.; Rancatore, B. J.; Thorkelsson, K.; Xu, T.; Liu, Z.; Wang, L.-W.; Liu, Y.; Alivisatos, A. P. *ACS Nano* **2014**, *8* (3), 2532−2540.
(29) Gupta, S.; Zhang, Q.; Emrick, T.; Balazs, A. C.; Russell, T. P. *Nat. Mater.* **2006**, *5* (3), 229−233.
(30) Jang, S. G.; Kramer, E. J.; Hawker, C. J. *J. Am. Chem. Soc.* **2011**, *133* (42), 16986−16996.
(31) Lin, Y.; Daga, V. K.; Anderson, E. R.; Gido, S. P.; Watkins, J. J. *J. Am. Chem. Soc.* **2011**, *133* (17), 6513−6516.
(32) Jang, S. G.; Khan, A.; Hawker, C. J.; Kramer, E. J. *Macromolecules* **2012**, *45* (3), 1553−1561.
(33) Yao, L.; Lin, Y.; Watkins, J. J. *Macromolecules* **2014**, *47* (5), 1844−1849.
(34) Song, D.-P.; Lin, Y.; Gai, Y.; Colella, N. S.; Li, C.; Liu, X.-H.; Gido, S.; Watkins, J. J. *J. Am. Chem. Soc.* **2015**, *137* (11), 3771−3774.
(35) Warren, S. C.; Messina, L. C.; Slaughter, L. S.; Kamperman, M.; Zhou, Q.; Gruner, S. M.; DiSalvo, F. J.; Wiesner, U. *Science* **2008**, *320* (5884), 1748−1752.
(36) Yeh, S.-W.; Wei, K.-H.; Sun, Y.-S.; Jeng, U. S.; Liang, K. S. *Macromolecules* **2003**, *36* (21), 7903−7907.
(37) Yeh, S.-W.; Wei, K.-H.; Sun, Y.-S.; Jeng, U. S.; Liang, K. S. *Macromolecules* **2005**, *38* (15), 6559−6565.
(38) Kim, B. J.; Chiu, J. J.; Yi, G. R.; Pine, D. J.; Kramer, E. J. *Adv. Mater.* **2005**, *17* (21), 2618−2622.
(39) Park, M. J.; Char, K.; Park, J.; Hyeon, T. *Langmuir* **2006**, *22* (4), 1375−1378.
(40) Chung, H.-J.; Ohno, K.; Fukuda, T.; Composto, R. J. *Nano Lett.* **2005**, *5* (10), 1878−1882.
(41) Li, L.; Miesch, C.; Sudeep, P. K.; Balazs, A. C.; Emrick, T.; Russell, T. P.; Hayward, R. C. *Nano Lett.* **2011**, *11* (5), 1997−2003.
(42) Kao, J.; Bai, P.; Chuang, V. P.; Jiang, Z.; Ercius, P.; Xu, T. *Nano Lett.* **2012**, *12* (5), 2610−2618.
(43) Kao, J.; Thorkelsson, K.; Bai, P.; Zhang, Z.; Sun, C.; Xu, T. *Nat. Commun.* **2014**, *5*, 4053.
(44) Rancatore, B. J.; Mauldin, C. E.; Fréchet, J. M. J.; Xu, T. *Macromolecules* **2012**, *45* (20), 8292−8299.
(45) Kim, S. H.; Misner, M. J.; Xu, T.; Kimura, M.; Russell, T. P. *Adv. Mater.* **2004**, *16* (3), 226−231.
(46) Ruokolainen, J.; Saariaho, M.; Ikkala, O.; ten Brinke, G.; Thomas, E. L.; Torkkeli, M.; Serimaa, R. *Macromolecules* **1999**, *32* (4), 1152−1158.
(47) Luyten, M. C.; Alberda van Ekenstein, G. O. R.; ten Brinke, G.; Ruokolainen, J.; Ikkala, O.; Torkkeli, M.; Serimaa, R. *Macromolecules* **1999**, *32* (13), 4404−4410.
(48) Peng, S.; Lee, Y.; Wang, C.; Yin, H.; Dai, S.; Sun, S. *Nano Res.* **2008**, *1* (3), 229−234.

DOI: 10.1021/jacs.5b02494
J. Am. Chem. Soc. 2015, 137, 6356−6365